

UNIVERSIDAD DE LOS ANDES  
FACULTAD DE INGENIERÍA Y CIENCIAS APLICADAS



TÍTULO TESIS

LUKAS WOLFF CASANOVA

TESIS PARA OPTAR AL GRADO DE  
MAGÍSTER EN CIENCIAS DE LA INGENIERÍA

PROFESOR GUÍA: PATRICIO MORENO

PROFESOR Co-GUÍA: ALVARO PAUL

PROFESOR Co-GUÍA: JORGE GOMEZ

SANTIAGO, AGOSTO DE 2023



# **Devotion**

## **Abstract**

## Acknowledgements

# Contents

# List of Figures

# List of Tables

# Chapter 1

## Introduction

Concrete is ubiquitous: it can be found in every house, town, city, and country, regardless of the level of development, wealth, or political foundation of the region. It is such a versatile material—initially fluid, but hardening over time into a rock-like solid—that it can be used in countless applications, from the foundation of a small house to the construction of bridges and skyscrapers. Concrete is composed of three main components: cement, water, and aggregates (such as sand, gravel, or stone). Together, these elements constitute the most widely used construction material worldwide, with global demand projected to increase by approximately 12% - 23% by 2050 (?).

Cement production alone is responsible for 8% of global  $CO_2$  emissions (?). When the water demand and the emissions from construction activities are also considered, it becomes clear that concrete production accounts for a significant percentage of annual  $CO_2$  emissions worldwide. For this reason, several restrictions and sustainable practices are being adopted, such as the use of recycled aggregates or alternative cementitious materials (e.g., fly ash, slag, or silica fume), which reduce the amount of cement required in concrete production and extend the service life of structures.

Concrete exhibits excellent compressive strength (around 30 MPa) but relatively poor tensile strength (around 3 MPa). To overcome this limitation, steel reinforcement is commonly used to enhance tensile resistance. However, reinforcement introduces durability issues, as steel is prone to corrosion. Chlorides can penetrate the porous structure and microcracks of the concrete, leading to steel corrosion, a reduction in structural integrity, and increased maintenance costs.

Ultra-High-Performance Concrete (UHPC) has been developed to address these chal-

lenges, with the aim of improving durability and extending the lifespan of concrete structures. UHPC is characterized by very high compressive strength (around 150 MPa), extremely low permeability, and excellent resistance to environmental factors such as freeze-thaw cycles and chemical attack. These properties are achieved by incorporating high-quality materials such as silica fume, superplasticizers, and steel fibers, which greatly enhance the mechanical and durability performance of the composite. Silica fume, superplasticizers, and a well-graded aggregate system increase the density of the cementitious matrix, lowering the water-to-cement ratio and reducing internal voids. This densification enhances the overall compactness of the concrete, leading to higher compressive strength and reduced permeability, due to the significant decrease in porosity. Steel fibers, in turn, are incorporated to improve the tensile behavior of UHPC (typically around 15 MPa) by providing distributed reinforcement throughout the matrix. Their inclusion has been shown to substantially enhance the post-cracking performance of the material [CITAR], allowing it to sustain higher loads and larger deformations without brittle failure. Nevertheless, the effectiveness of steel fibers strongly depends on their orientation and dispersion within the cementitious matrix. Undesirable alignment or clustering can significantly limit their contribution, reducing the tensile strength and overall efficiency of UHPC.

Currently, the study of steel fiber behavior relies primarily on experimental methods, where full-scale (1:1) specimens are tested under controlled conditions to analyze fiber orientation under specific circumstances. While valuable, this methodology is highly inefficient: it involves substantial costs, lacks scalability, and does not allow for rapid iteration across multiple variables.

To address these limitations, multiphase computational fluid dynamics (CFD) simulations are proposed as a more effective approach for investigating fiber behavior. CFD simulations make it possible to iteratively explore the influence of intrinsic UHPC properties, such as rheology, as well as external factors, including placement techniques, mold geometry, or container dimensions.

To validate the proposed CFD simulation, it is necessary to obtain experimental data of UHPC in its fresh state. For this purpose, Particle Image Velocimetry (PIV) will be employed, as currently implemented at the university by Cristóbal Maggy and Valentina Tapia. In addition, it is also essential to analyze how steel fibers behave within the

fluid matrix, for which the Particle Tracking Velocimetry (PTV) technique must be self-implemented.

AGREGAR LIMITACIONES DE ESTUDIO

# Chapter 2

## Bibliographic Revision

Throughout this section, a comprehensive review of the literature will be provided. Based on the L-shape model proposed by (?) to study UHPC flow dynamics, as illustrated in Figure ?? the discussion will focus on the fundamental principles, experimental methodologies, and numerical approaches. Particular emphasis will be placed on Particle Image Velocimetry (PIV) and Particle Tracking Velocimetry (PTV) techniques, along with Discrete Element Method (DEM) and Computational Fluid Dynamics (CFD) frameworks, which together provide the experimental and numerical foundations for analyzing fiber dynamics in viscoplastic media.

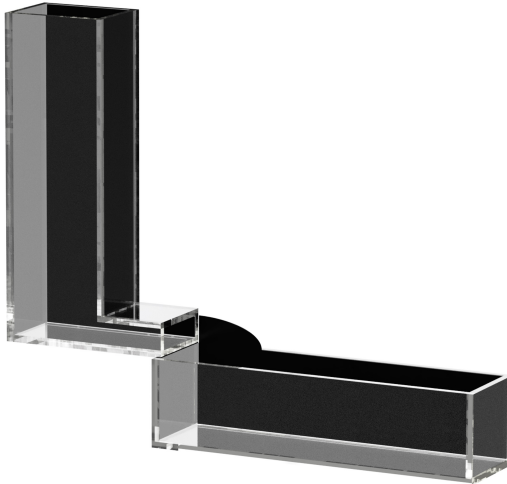


Figure 2.1: L-shape model for UHPC flow analysis  
Source: Author's own elaboration.

## 2.1 Multiphase Flow Simulation

To simulate the behavior of UHPC, a transparent non-Newtonian fluid with tunable rheological properties, known as Carbopol, is employed. As demonstrated by (?) Carbopol can effectively replicate the flow properties of UHPC. Furthermore, recent work by (?) has provided a deeper understanding of its behavior under different shear rates and temperatures, offering valuable insights for the simulation process. The rheological properties of Carbopol obtained by Tapia, V. are presented in Figure ?? where two concentrations of the fluid (0.2% and 0.5%) were tested.

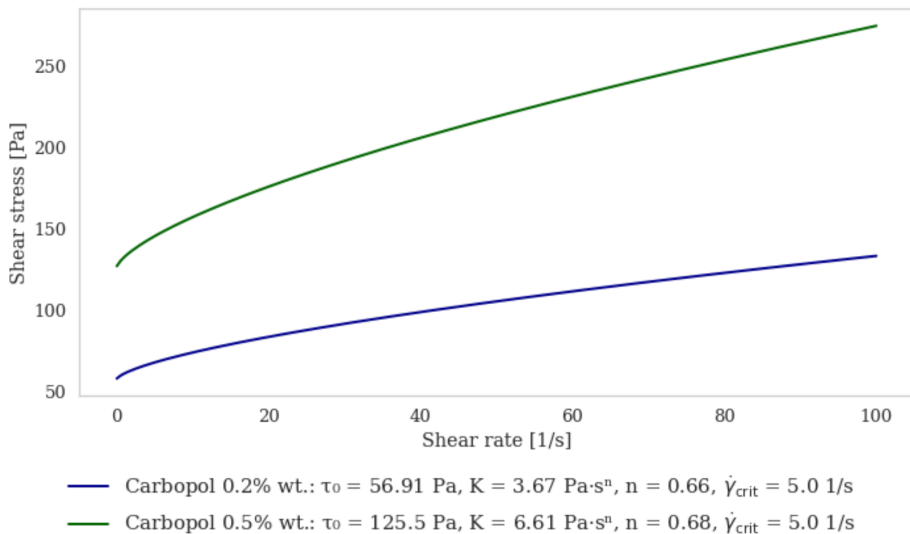


Figure 2.2: Rheological properties of Carbopol at different concentrations  
 Source: Tapia, V. (2025)

### 2.1.1 Fluid Phase (CFD)

Computational Fluid Dynamics (CFD) was originally formalized by (?) where three fundamental conservation laws were considered: (i) the law of conservation of mass (transport of mass), (ii) Newton's second law of motion (transport of momentum), and (iii) the law of conservation of energy (transport of energy). These are expressed in the following equations, respectively:

$$\frac{\partial \rho}{\partial t} + \nabla \cdot (\rho \mathbf{u}) = 0 \quad (2.1)$$

$$\rho \left( \frac{\partial \mathbf{u}}{\partial t} + \mathbf{u} \cdot \nabla \mathbf{u} \right) = -\nabla p + \mu \nabla^2 \mathbf{u} + \rho \mathbf{g} \quad (2.2)$$

$$\rho \frac{De}{Dt} = -p \nabla \cdot \mathbf{u} + \Phi + \nabla \cdot (k \nabla T) \quad (2.3)$$

Together, these equations form the basis of the Navier–Stokes equations, which govern the motion of fluid substances. For clarity, the same laws can also be written in index notation:

$$\frac{\partial \rho}{\partial t} + \frac{\partial(\rho u_i)}{\partial x_i} = 0 \quad (2.4)$$

$$\rho \left( \frac{\partial u_i}{\partial t} + u_j \frac{\partial u_i}{\partial x_j} \right) = -\frac{\partial p}{\partial x_i} + \frac{\partial}{\partial x_j} \left[ \mu \left( \frac{\partial u_i}{\partial x_j} + \frac{\partial u_j}{\partial x_i} \right) + \lambda \frac{\partial u_k}{\partial x_k} \delta_{ij} \right] + \rho g_i \quad (2.5)$$

To solve the Navier-Stokes equations across the entire computational domain, the fluid must be discretized into finite volume elements, which allows the equations to be approximated using numerical methods. The accuracy of this process is determined by the shape, size, and arrangement of the elements; therefore, it is crucial to optimize the mesh to achieve high accuracy while minimizing computational cost, since the Navier-Stokes equations need to be solved within each cell.

### 2.1.2 Fiber Phase (DEM)

Based on Newton's law of motion, a rod like particle motion equation can be expressed as:

$$m \frac{dv}{dt} = \sum F_c + F_d + F_b + mg \quad (2.6)$$

$$I \frac{d\omega}{dt} = \sum T_c \quad (2.7)$$

To simulate the behavior of rod-like particles, a DEM framework is implemented within a CFD non-resolved simulation, where various analytical methods have been developed to estimate and detect contacts and forces on non-spherical particles. As proposed by (?) a method is used in which an elongated particle is represented by a set of spheres,

or ellipsoids, proposed by (?) based on the following equations:

$$\left( \left| \frac{x}{a} \right|^{s_2} + \left| \frac{y}{b} \right|^{\frac{s_1}{s_2}} \right)^{\frac{s_1}{s_2}} + \left| \frac{z}{c} \right|^{s_1} = 1 \quad (2.8)$$

A Discrete Element Method (DEM) framework to simulate the behavior of rod-like particles was proposed by (?) reducing the particles' motion to translational and rotational components, as described by:

$$m_i \frac{dv_i}{dt} = \sum F_{c,i} + m_i g + f_{pf,i} \quad (2.9)$$

$$\frac{d(I_i \omega_i)}{dt} = R_i \cdot (\sum M_{c,i} + M_{pf,i}) \quad (2.10)$$

### 2.1.3 Phases Integration

HABLAR DE COMO SE COMBINAN LOS METODOS ENFATIZANDO EN EL QUE SE USARA

To validate both, fluid and particle motion, PIV and PTV experimental methodologies where implemented, as provide a non-intrusive solution to measure velocity fields and particle trajectories, respectively.

### 2.1.4 Particle Image Velocimetry

Particle Image Velocimetry (PIV) is an optical flow visualization technique used to obtain instantaneous velocity measurements and related properties in fluids, enabling the reconstruction of Eulerian velocity fields (?) through image correlation methods. The fluid is seeded with tracer particles that are assumed to accurately follow the flow dynamics. These particles are illuminated by a laser sheet, as shown in Figure ?? which presents the setup implemented by (?) at Universidad de los Andes. The particle motion is captured using a high-speed camera, and the recorded images are subsequently analyzed to determine the velocity field of the fluid.

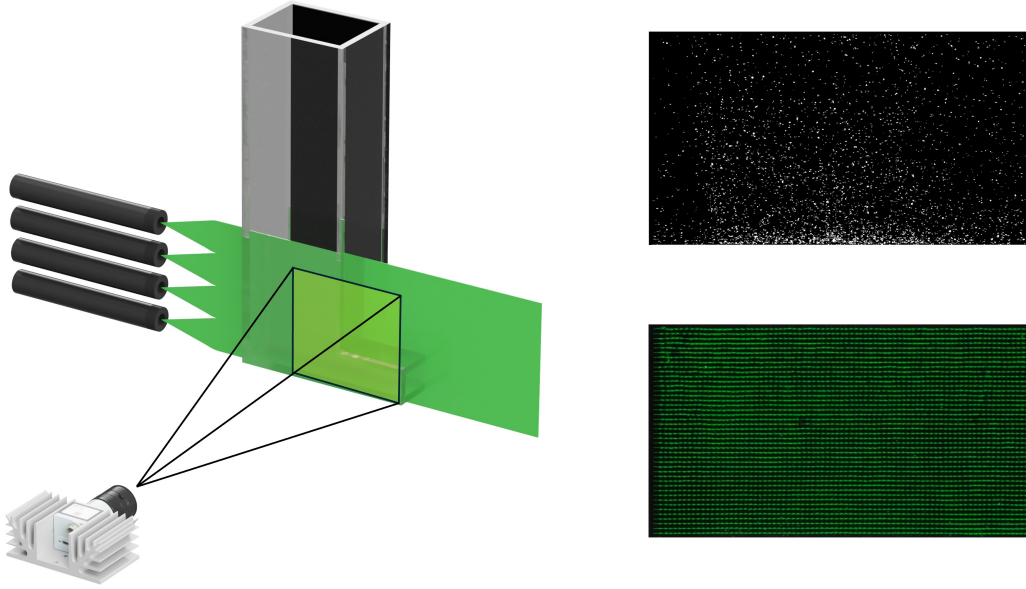


Figure 2.3: PIV setup based on the L-Shape model  
Source: Author's own elaboration.

## 2.2 Particle Tracking Velocimetry

While PIV enables the study of Eulerian velocity fields, Particle Tracking Velocimetry (PTV) provides a Lagrangian perspective, resolving the motion of individual particles with high temporal resolution (?).

Although PIV used an illuminated plane to capture the motion of particles, PTV requires a volumetric approach to accurately track the three-dimensional trajectories and rotation of particles. Thus, and based on the PIV setup, volumetric illumination leds were used to capture the motion of particles within a defined volume, as Figure ?? shows.

### 2.2.1 Particle Detection

Several methodologies have been developed for particle detection in PTV, ranging from traditional computational algorithms such as the Hough Transform, Canny filtering, and edge detection, as reviewed in (?) to more recent approaches based on deep learning, which have demonstrated superior reliability compared to classical methods (?). In particular, segmentation models have shown strong robustness and performance, as

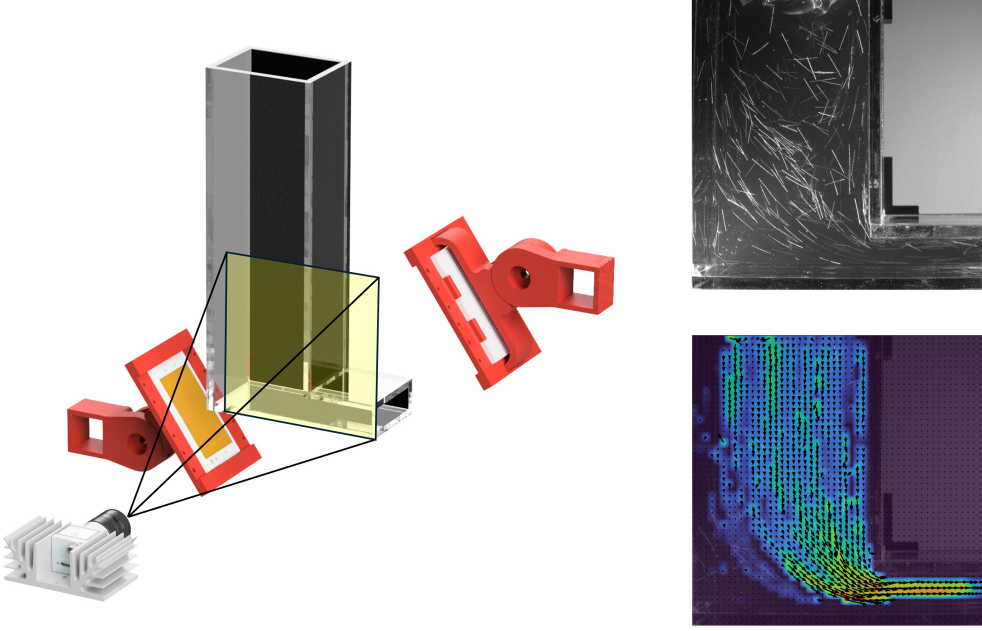


Figure 2.4: PTV setup based on volumetric illumination  
Source: Author's own elaboration.

reported by (?) where a YOLO-based model was successfully applied to small rod-like particles. Throughout this work, conventional algorithms are compared with deep learning-based models to assess their effectiveness in detecting and tracking UHPC fibers in a viscoplastic medium.

The performance of these detection methodologies is often evaluated using confusion matrices, which provide a comprehensive overview of the model's predictive capabilities. These matrices summarize the counts of true positives (TP), false positives (FP), true negatives (TN), and false negatives (FN), allowing for the calculation of key metrics such as precision, recall, F1-score and Intersection over Union (IoU) as (?) defined:

$$\text{Precision} = \frac{TP}{TP + FP} \quad (2.11)$$

$$\text{Recall} = \frac{TP}{TP + FN} \quad (2.12)$$

$$\text{F1 Score} = 2 \cdot \frac{\text{Precision} \cdot \text{Recall}}{\text{Precision} + \text{Recall}} \quad (2.13)$$

$$\text{IoU} = \frac{TP}{TP + FP + FN} \quad (2.14)$$

## 2.2.2 Particle Tracking

Once particles are detected, they need to be linked across consecutive frames. Based on the characteristics and motion of each rod-like particle, it becomes possible to reliably identify and track individual fibers over time. Several tracking methods have been developed for this purpose, including nearest-neighbor approaches, Kalman filtering, and more advanced deep learning-based techniques. In the present work, an  $\alpha$ - $\beta$ - $\gamma$  filter (?) and (?) derived from the Kalman filter (?) was implemented. This filter uses the known state of an object  $Z_n$  (position, velocity, and acceleration) together with a prediction-correction scheme to estimate its future state, based on the present state  $\hat{X}_{n,n-1}$ , while continuously updating the prediction by incorporating new measurements. This approach allows for robust tracking of fibers even in the presence of noise or partial occlusions.

$$\hat{X}_{n,n-1} = \hat{X}_{n-1,n-1} + K_n \cdot (Z_n - \hat{X}_{n,n-1}) \quad (2.15)$$

$K_n$  is known as Kalman gain, which determines the weight given to the new measurement versus the prediction. The filter parameters  $\alpha$ ,  $\beta$ , and  $\gamma$  control the responsiveness of the filter to changes in position, velocity, and acceleration, respectively both lineal and angular movements:

$$\hat{X}_{n,n-1} = \hat{X}_{n-1,n-1} + \alpha \cdot (Z_n - \hat{X}_{n,n-1}) \quad (2.16)$$

$$\dot{\hat{X}}_{n,n-1} = \dot{\hat{X}}_{n-1,n-1} + \beta \cdot (Z_n - \hat{X}_{n,n-1}) / \Delta t \quad (2.17)$$

$$\ddot{\hat{X}}_{n,n-1} = \ddot{\hat{X}}_{n-1,n-1} + \gamma \cdot (Z_n - \hat{X}_{n,n-1}) / (2 \cdot \Delta t^2) \quad (2.18)$$

Then, it is necessary update the model to time variation between each frame, as all the variables experience a change, basic dynamic equation should be applied to obtain the corresponding data as the followings equations show:

$$\hat{X}_{n,n} = \hat{X}_{n,n-1} + \dot{\hat{X}}_{n,n-1} \cdot \Delta t + \frac{1}{2} \cdot \ddot{\hat{X}}_{n,n-1} \cdot \Delta t^2 \quad (2.19)$$

$$\dot{\hat{X}}_{n,n} = \dot{\hat{X}}_{n,n-1} + \ddot{\hat{X}}_{n,n-1} \cdot \Delta t \quad (2.20)$$

$$\ddot{\hat{X}}_{n,n} = \ddot{\hat{X}}_{n,n-1} \quad (2.21)$$

Therefore, it is possible to take the current fiber parameters and use them as input for the  $\alpha$ - $\beta$ - $\gamma$  filter for each fiber, where  $\Delta t = 1/fps$ . This will output a virtual fiber corresponding to each fiber recognized in the previous frame. The virtual fiber that satisfies all the criteria will be linked to the newly detected fiber. Additionally, when each particle is first detected, the initial linear and angular velocity and the acceleration are assumed to be zero, regardless of the time instant.

# Chapter 3

## Methodology

### 3.1 Particle Tracking Velocimetry Implementation

PTV is typically structured into three main steps, as illustrated in Figure ??: (i) particle detection, (ii) particle characterization, and (iii) particle tracking. Following these stages, a post-processing step is performed to refine the results and enhance the quality of the data analysis.

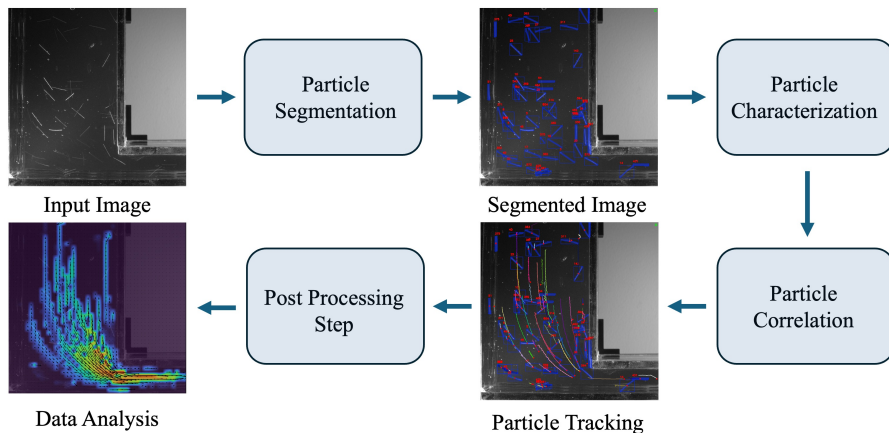


Figure 3.1: PTV flowchart  
Source: Author's own elaboration.

Since UHPC fibers often exhibit non-uniform surface properties, the light they reflect may vary along their length or be affected by suboptimal alignment with respect to the light source (see Figure ??). Consequently, conventional detection methods proved inadequate. To overcome this limitation, deep learning-based approaches were tested, as the literature has demonstrated their effectiveness in detecting small rod-like particles.

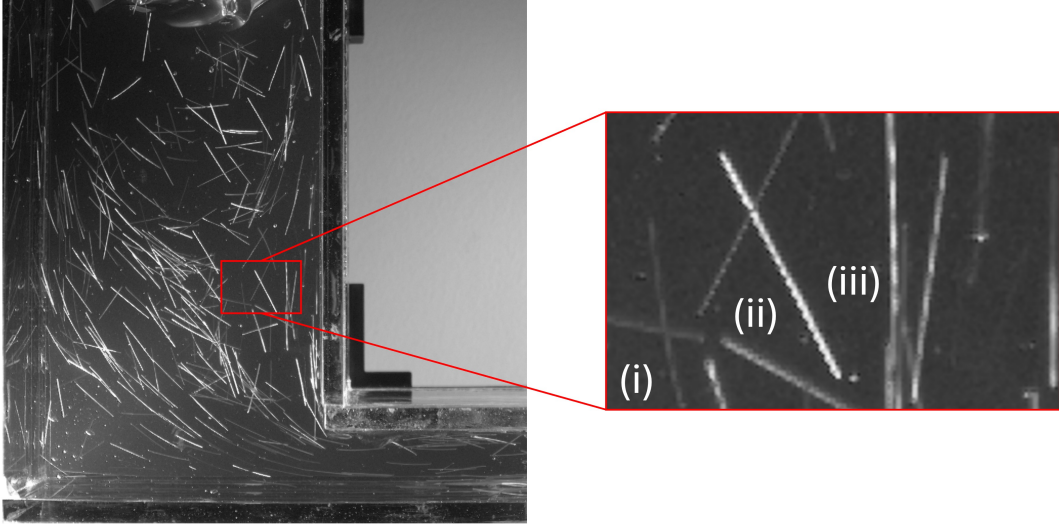


Figure 3.2: Examples of fiber light reflection: (i) a group of fibers with suboptimal alignment relative to the light source, (ii) a well-illuminated fiber, and (iii) a fiber exhibiting non-uniform light reflection along its length.

Source: Author's own elaboration.

The Hough Transform was compared with YOLOv11 and SAM2 to evaluate their performance in detecting and tracking UHPC fibers. Both YOLO and SAM were trained using the same dataset, which consisted of two sets of images: (i) a low-density case with few fibers and no overlapping, and (ii) a high-density case with a larger number of fibers and overlapping, as Figure ?? shows.

The results showed that the Hough Transform achieved low detection accuracy. Although some fibers were correctly identified as true positives (TP), the method also produced a high number of false positives (FP). In contrast, YOLOv11 demonstrated high precision, successfully detecting overlapping fibers while maintaining a low FP rate, as evidenced by the confusion matrix in Figure REFERENCIAR. Finally, SAM2 failed to produce any valid detections, resulting in all evaluation metrics being zero, as

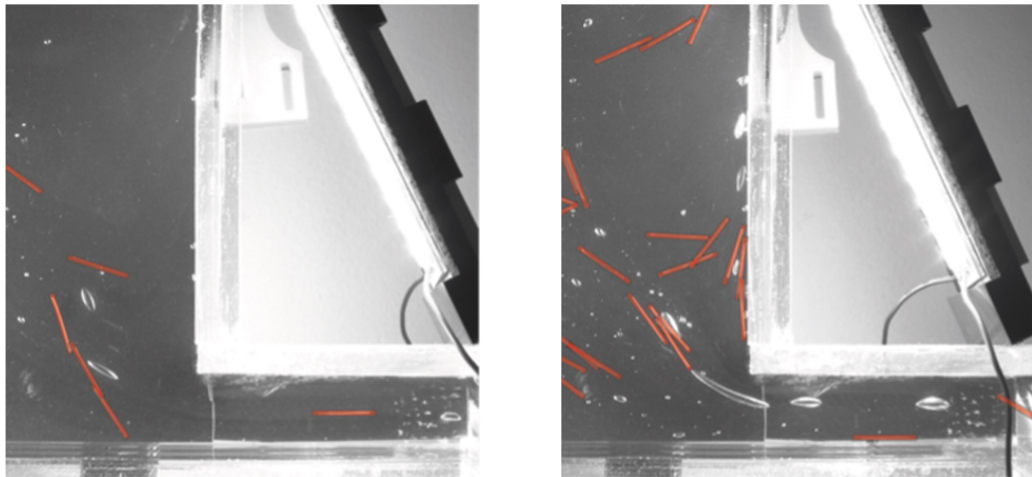


Figure 3.3: Representative examples from the training dataset: (a) image with a low concentration of well-separated fibers; (b) image with a high concentration of overlapping fibers and a significant presence of bubbles.

Source: Author's own elaboration.

summarized in Table REFERENCIAR.

# Nomenclature

## Bibliography

- Auernhammer, G. K., Fataei, S., Haustein, M. A., Patel, H. P., Schwarze, R., Secrieru, E., & Mechtcherine, V. (2020). Transparent model concrete with tunable rheology for investigating flow and particle-migration during transport in pipes. *Materials & Design*, 193, 108673.
- Cheng, D., Reiner, D. M., Yang, F., Cui, C., Meng, J., Shan, Y., Liu, Y., Tao, S., & Guan, D. (2023). Projecting future carbon emissions from cement production in developing countries. *Nature Communications*, 14(1), 8213.
- Cundall, P. A. & Strack, O. D. (1979). A discrete numerical model for granular assemblies. *geotechnique*, 29(1), 47–65.
- Everingham, M., Eslami, S. A., Van Gool, L., Williams, C. K., Winn, J., & Zisserman, A. (2015). The pascal visual object classes challenge: A retrospective. *International journal of computer vision*, 111(1), 98–136.
- Favier, J. F., Abbaspour-Fard, M. H., Kremmer, M., & Raji, A. O. (1999). Shape representation of axi-symmetrical, non-spherical particles in discrete element simulation using multi-element model particles. *Engineering computations*, 16(4), 467–480.
- Gray, J. & Murray, W. (1993). A derivation of an analytic expression for the tracking index for the alpha-beta-gamma filter. *IEEE Transactions on Aerospace and Electronic Systems*, 29(3), 1064–1065.
- Huang, H., Gao, X., Li, L., & Wang, H. (2018). Improvement effect of steel fiber orientation control on mechanical performance of uhpc. *Construction and Building Materials*, 188, 709–721.
- Maas, H.-G., Gruen, A., & Papantoniou, D. (1993). Particle tracking velocimetry in three-dimensional flows: Part 1. photogrammetric determination of particle coordinates. *Experiments in fluids*, 15(2), 133–146.
- Maggi, C. A. (2023). Sistema de velocimetría de imágenes de partículas. Trabajo de titulación para optar al título de ingeniero civil eléctrico, Universidad de los Andes, Santiago, Chile. Profesor Guía: Gustavo Luis Funes.

- Plaksyyi, A., Skublewska-Paszkowska, M., & Powroźnik, P. (2023). A comparative analysis of image segmentation using classical and deep learning approach. *Advances in Science and Technology Research Journal*, 17(6), 127–139.
- Qamar, S., Baba, A., Verger, S., & Andersson, M. (2024). Segmentation and characterization of macerated fibers and vessels using deep learning. arxiv. *arXiv preprint arXiv:2401.16937*.
- Raffel, M., Willert, C. E., Scarano, F., Kähler, C. J., Wereley, S. T., & Kompenhans, J. (2018). *Particle image velocimetry: a practical guide*. Springer.
- Roache, P. J. (1972). *Computational Fluid Dynamics*. Albuquerque, NM: Hermosa Publishers.
- Seyfi, S., Karimpour, S., & Balachandar, R. (2024). Simultaneous flow and particle measurements for multiphase flows in hydraulic engineering: A review and synthesis of current state. *Flow Measurement and Instrumentation*, 99, 102666.
- Tapia, V. A. (2025). Experimental analysis of fiber-fluid dynamics in viscoplastic media using piv. Trabajo de titulación para optar al título de magister en ciencias de la ingeniería, Universidad de los Andes, Santiago, Chile. Profesor Guía: Patricio Moreno.
- Tenne, D. & Singh, T. (2000). Optimal design of  $\alpha$ - $\beta$ - $\gamma$  filters. *Proceedings of the American Control Conference*, 6, 4348 – 4352 vol.6.
- Welch, G., Bishop, G., et al. (1995). An introduction to the kalman filter.
- Williams, J. R. & Pentland, A. P. (1992). Superquadrics and modal dynamics for discrete elements in interactive design. *Engineering Computations*, 9(2), 115–127.
- Winnefeld, F., Leemann, A., German, A., & Lothenbach, B. (2022). Co2 storage in cement and concrete by mineral carbonation. *Current Opinion in Green and Sustainable Chemistry*, 38, 100672.